Dalton Transactions

ROYAL SOCIETY OF CHEMISTRY

PAPER

View Article Online
View Journal

Cite this: DOI: 10.1039/d6dt00320f

A novel family of heteroleptic 1D chain spin-crossover complexes and its DFT modelling. How the formation of polynuclear chains modifies the ligand-field effects on spin transition

Vladyslav Maliuzhenko,[a] Marek Weselski,[a] Maria Książek,[b] Tim Hochdörffer,[c] Juliusz A. Wolny,*[c] Volker Schünemann,[c] Joachim Kusz[b] and Robert Bronisz *[a]

Reactions of the ditopic ligands 1-(5-(2-pyridyl)tetrazol-1-yl)-3-(tetrazol-2-yl)propane (5-p1tz2tz), 1-(5-(2-pyridyl)tetrazol-2-yl)-3-(tetrazol-2-yl)propane (5-p2tz2tz), and 1-(3-(2-pyridyl)-1,2,4-triazol-1-yl)-3-(tetrazol-1-yl)propane (3-p1tr1tz) with iron(II) tetrafluoroborate afforded a series of one-dimensional coordination polymers: $[Fe(5\text{-}p1tz2tz)_2](BF_4)_2$ (**1**), $[Fe(5\text{-}p2tz2tz)_2](BF_4)_2$ (**2**), $[Fe(3\text{-}p1tr1tz)_2](BF_4)_2{\cdot}CH_3CN$ (**3**) and $[Fe(3\text{-}p1tr1tz)_2](BF_4)_2{\cdot}CH_3OH$ (**4**). The first coordination spheres of all complexes are composed of two chelating pyridylazole units and two tetrazole rings. The two complexes involving pyridyltetrazole-form 1D chains with *trans*-coordinated monotetrazoles. They exhibit gradual spin transitions centred at approximately 350 K. For the pyridyl-1,2,4-triazole ligand, two polymorphs were isolated. One compound is a structural analogue of pyridyltetrazole complexes and exhibits high-spin down to 10 K. Modifying the synthetic procedure yields a 1D zig-zag chain with almost the same molecular volume, but with *cis*-co-ordinated monodentate tetrazole. This complex exhibits an abrupt spin-crossover accompanied by a hysteresis loop ($T_{1/2}$ = 114 K, $T_{1/2}$ = 131 K). Density functional theory (DFT) modelling of the above systems, combined with results for known mononuclear and polynuclear complexes of 1-propyltetrazole revealed how the spin-transition energies vary from the mononuclear species to the corresponding 1D chains.

Received 6th February 2026,
Accepted 13th May 2026

DOI: 10.1039/d6dt00320f

rsc.li/dalton

Introduction

Donor groups play a crucial role in defining donor–acceptor properties, while also determining the structural properties of coordination compounds. One group of compounds whose properties depend extremely strongly on these features is that of coordination compounds exhibiting the spin-crossover (SCO) phenomenon.[1] The structural diversity required for the discovery of novel compounds can be achieved using ligands, which can lead to both homoleptic and heteroleptic systems. One way of creating heteroleptic coordination compounds is to use asymmetric ditopic ligands. The relative position of the donor atoms determines whether ditopic ligands serve as chelating molecules in mononuclear species, as molecules that bind a limited number of metal ions into oligonuclear products, or as bridging units that result in coordination polymers.

The chelating molecule 2-(1,2,4-triazol-3-yl)pyridine (Hpt) creates the Fe(II) mononuclear systems $[Fe(Hpt)_3](BF_4)_2{\cdot}2H_2O$[2] and $[Fe(Hpt)_3]SO_4{\cdot}0.4BF_4{\cdot}3H_2O$.[3] Substituted 3-(1,2,4-triazol-3-yl)pyridine-type ligands also reveal great suitability for forming Fe(II) SCO complexes.[4] Linking an additional pyridine ring possessing nitrogen donor atoms in the *meta*[5] or *para*[6] positions with 1,2,4-triazole backbones enables the formation of SCO coordination polymers. Derivatives containing additional 4-(3-pyridyl)phenyl[7] or 4-(4-pyridyl)phenyl[8] substituents also exhibit this ability. For comparison, ligands containing two directly joined 2-(1,2,4-triazol-3-yl)pyridine units have been used to successfully prepare coordination polymers.[9] The structure and properties of various types of Fe(II) complexes containing more complex ligands based on conjugated 1,2,4-triazole and tetrazole donors have been reviewed in detail.[10,11]

It should be noted at this point that the effect of changing the effective donor properties of the ligands from mononuclear to polynuclear SCO species is of key importance. This change is one of the most important issues in crystal engineering of SCO materials. Straightforward manipulation of the ligand environment to create heteroleptic complexes inevitably

[a]Faculty of Chemistry, University of Wrocław, F. Joliot-Curie 14, 50-383 Wrocław, Poland. E-mail: robert.bronisz@uwr.edu.pl
[b]Institute of Physics, University of Silesia, 75 Pułku Piechoty 1, 41-500 Chorzów, Poland
[c]Department of Physics, RPTU Kaiserslautern-Landau, Erwin Schrödinger Str. 46, 67663 Kaiserslautern, Germany

results in ligand scrambling, producing a mixture of stereoisomers for mononuclear complexes. Using ditopic ligands gives more defined, higher-nuclearity systems and tunes the spin-transition electronic energy, *i.e.* the effective ligand-field splitting. This effect complicates the rational design of SCO materials.

This is clearly evident even in the homoleptic complexes of 1-alkyl tetrazoles. They typically act as monodentate coordinating donors; an important example is the $[Fe(ptz)_6](BF_4)_2$ (ptz = 1-*n*-propyl-tetrazole).[12–14] They were subsequently exploited intensively to design bridging ligands suitable for constructing coordination polymers. Studies on the use of 1,2-di(tetrazol-1-yl)alkanes as bridging ligands, in which the donor groups are separated by an increasing distance *via* an alkyl linker, have shown that increasing the flexibility of the bridging ligand decreases the cooperativity of SCO.[15–17] Expanding the research to include 1,2-di(1,2,3-triazolyl)alkanes, particularly their disubstituted derivatives, has revealed that the presence of conformationally labile fragments can result in unusual and rare phenomena, such as reverse[18] or multiway spin transitions.[19]

As the use of bisazoles leads to coordination polymers rather than mononuclear systems, in which separate donors coordinate with neighbouring metal ions, we opted for a polymeric approach when designing the first coordination sphere. In this approach, two different coordinating parts are linked by a flexible spacer.[20] The first part coordinates bidentately as 1,2,4-triazole-pyridine or tetrazolepyridine; the second part coordinates monodentately as *N*-alkyltetrazole. Thus, the aim of the study was to investigate the coordination properties of heteroleptic ligands able to form Fe(II) SCO systems. In particular, the manner of organizing the composition of the first coordination sphere in the presence of two types of donors: a chelating and a monodentately coordinating one, linked by a flexible alkyl spacer.

This report presents an application involving three bridging ligands: 1-(5-(2-pyridyl)tetrazol-1-yl)-3-(tetrazol-2-yl)propane (5-p1tz2tz), 1-(5-(2-pyridyl)tetrazol-2-yl)-3-(tetrazol-2-yl)propane (5-p2tz2tz), and 1-(3-(2-pyridyl)-1,2,4-triazol-1-yl)-3-(tetrazol-1-yl)propane (3-p1tr1tz). These are used to prepare novel Fe(II) one-dimensional coordination polymers that exhibit various types of SCO transitions (see Scheme 1). The complexes exhibit SCO above room temperature (**1** and **2**), below room temperature (**3**), or remain in the HS form down to 10 K (**4**). The results of magnetic, single-crystal X-ray diffraction studies and DFT calculations are presented. The latter were applied to assess the change in spin-transition electronic energies when going from the mononuclear model to the 1D chain model. With the current level of DFT modelling of SCO complexes, it may be feasible to obtain a reliable estimation of the relevant factors (see references for a review).[21–23]

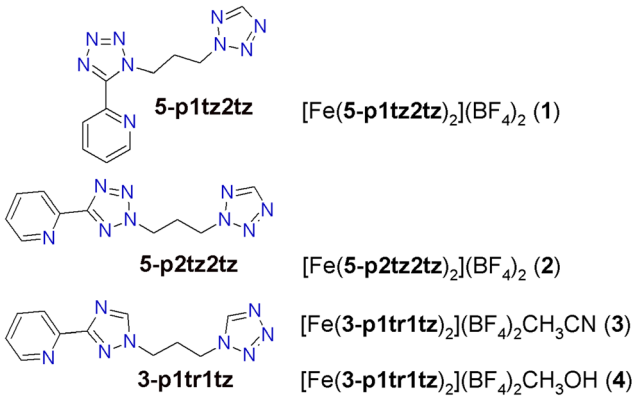

Scheme 1 Molecular structures of 5-p1tz2tz, 5-p2tz2tz and 3-p1tr1tz representing the ligands used in this work. Donor atoms are marked in blue.

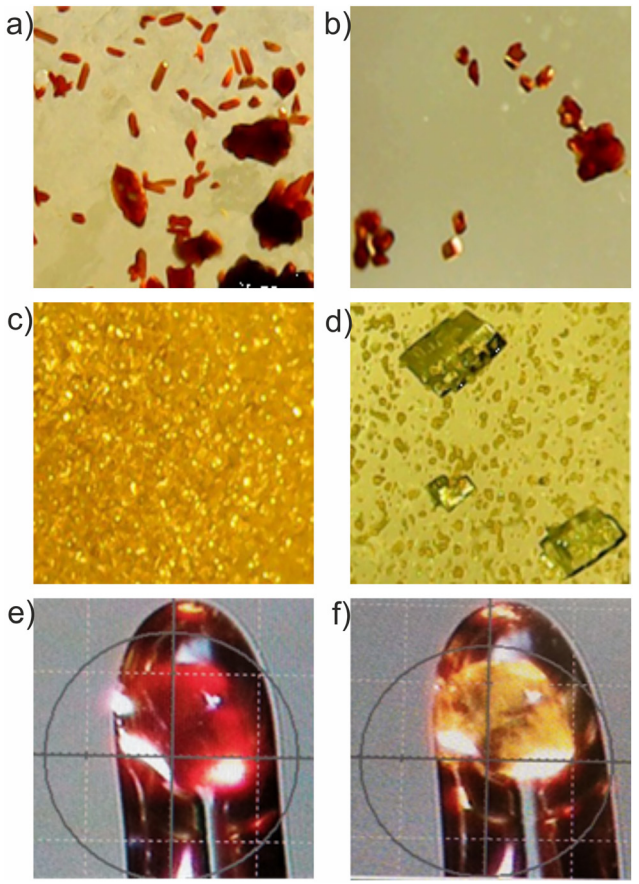

Fig. 1 View of crystals of **1** (a), **2** (b), **3** (c), and **4** (d) growing on the bottom of the Schlenk flask at room temperature as well as a single crystal of **2** at 250 K (LS form, e) and at 480 K (HS form, f).

Results and discussion

General characterisation

The complexes $[Fe(5\text{-p1tz2tz})_2](BF_4)_2$ (**1**, Fig. 1a) and $[Fe(5\text{-p2tz2tz})_2](BF_4)_2$ (**2**, Fig. 1b) were prepared by reacting 5-p1tz2tz[20] with iron(II) terafluoroborate in a 2 : 1 stoichiometric ratio in ethanol containing 3% water (v/v) and in anhydrous ethanol, respectively. The complexes exhibit high thermal stability, with decomposition starting above *ca.* 575 K (Fig. S1a) and above 550 K (Fig. S1b) for **1** and **2**, respectively.

The successful preparations of $[Fe(3\text{-p1tr1tz})_2](BF_4)_2{\cdot}CH_3CN$ (**3**, Fig. 1c) and $[Fe(3\text{-p1tr1tz})_2](BF_4)_2{\cdot}CH_3OH$ (**4**, Fig. 1d) were carried out in a 2 : 1 molar ratio in anhydrous acetonitrile and methanol, respectively. The FTIR spectrum of **3** shows a weak peak at 2247 cm^{-1}, indicating the presence of nitrile molecules (see Fig. S2c). A broad peak with a maximum at 3450 cm^{-1} appears in the FTIR spectrum of **4** (Fig. S2d), corresponding to an O–H stretching vibration. Thermogravimetric analysis of compounds **3** (see Fig. S1c) and **4** (see Fig. S1d) revealed a 6.3% and 3.7% loss in mass in the temperature range of 400–450 K, which corresponds to one acetonitrile and one methanol molecule, respectively, per formal complex molecule. Crystals of **1–4** are stable in air. It was established that heating crystals of **1** (Fig. 1e and f) and **2** involves a colour change from red to yellow. Cooling crystals of **3** in liquid nitrogen results in a deep red colour appearing. Thus, the observed thermochromism in **1–3** indicates the ability to undergo thermally induced SCO. In contrast, cooling the sample of **4** does not result in a change of yellow colour.

Magnetic and photomagnetic studies

Temperature-dependent magnetic susceptibility measurements were carried out on **1** in the range of 10–400 K. The thermal dependence of $\chi_M T$ is shown in Fig. 2a (χ_M, molar susceptibility; T, temperature). In the temperature range of 10–275 K, the complex remains in the low-spin (LS) form. Heating above 275 K involves a gradual transition to the high-spin (HS) state, whereas above 325 K it is more abrupt.

The shape of the $\chi_M T$ (T) dependence indicates that the SCO does not complete at 400 K, with $\chi_M T$ adopting a value of 3.2 cm^3 K mol^{-1}. The $\chi_M T$ (T) dependencies in cooling and heating modes are practically the same. The SCO behaviour of **2** is very similar to that found for **1**. Here, a more abrupt SCO begins above 300 K and does not finish at 400 K (see Fig. 2a). No hysteresis loop is observed.

Despite the high temperatures at which SCO occurs, the second cooling and heating cycles for **1** and **2** are practically identical relative to those recorded in the first cycle. Compared to **1** and **2**, which are based on the 5-(2-pyridyl)tetrazole fragment, **3** contains a 3-(2-pyridyl)-1,2,4-triazole unit, and its SCO properties differ significantly. Cooling sample **3** is accompanied by a very abrupt and complete spin transition at $T_{1/2}^{\downarrow}$ = 114 K (see Fig. 2b). In heating mode, the SCO shifts towards higher temperatures, with $T_{1/2}^{\uparrow}$ = 131 K, indicating a hysteresis loop width of 17 K.

The change of spin state from LS to HS in **3** can also be triggered by light irradiation at 520 nm. The metastable HS phase relaxes to the LS form above 50 K (T_{LIESST} = 69 K, see Fig. 2b). No switching from the LS to the HS phase caused by light (520 nm) is observed for **1** and **2**. Interestingly, **4**, in which acetonitrile has been replaced by methanol, does not exhibit SCO and remains in the HS form down to 10 K (see Fig. 2b). Light irradiation (808 nm) of sample **4** does not trigger HS → LS switching (r-LIESST). DSC studies of **1–3** (Fig. S3) revealed only thermal effects, which correspond to the results of the magnetic studies.

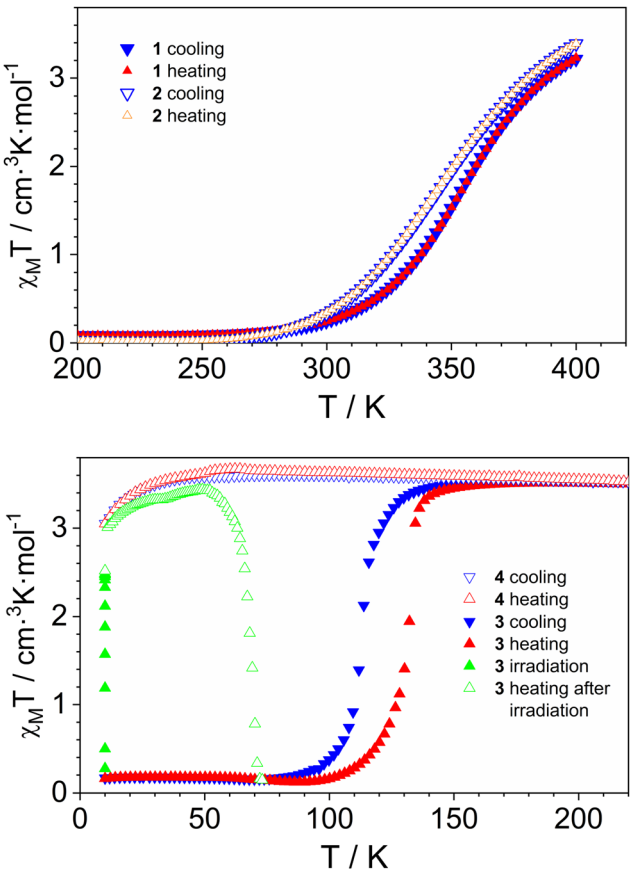

Fig. 2 $\chi_M T$ *vs.* T dependencies for **1** and **2** (a) and **3** and **4** (b) in cooling (blue) and heating (red) modes. Irradiation with laser light (λ = 520 nm) is denoted by green filled triangles whereas subsequent heating (0.3 K min^{-1}) is denoted by green open triangles.

Single-crystal X-ray diffraction studies

Crystal structures of 1 and 2. Complexes **1** and **2** crystallise in the triclinic $P\bar{1}$ space group (see the crystallographic data listed in Table S1). In **1**, two chelating 5-(2-pyridyl)tetrazole fragments coordinated with the metal ion through the nitrogen atoms of the pyridine ring (N1(py)) and the tetrazole ring ($N14(tz^{py})$) form an equatorial plane, whereas the axial positions of the coordination octahedron are occupied by tetrazole rings linked to the Fe(II) ion through exodentate nitrogen atoms (N24(tz)). At 100 K, the Fe–N distances characteristic of the LS form of Fe(II) range from 1.96 to 2.02 Å (see Table S2).

The octahedral geometry is distorted because of the coordination properties of the pyridyltetrazole. The N1(py)–Fe–N14(tz^{py}) bond angle is equal to 80.36(6)°. The N1(py)–Fe–N24(tz) and N14(tz^{py})–Fe–N24(tz) bond angles involving *trans*-arranged tetrazoles are close to 90° (Table S2). It is noticeable that the 5-(2-pyridyl)tetrazole fragment is non-planar and the torsion angle N1(py)–C2–C15–N14(tz^{py}) equals 6.987(3)°. Two iron(II) ions are bridged in such a way that the propylene(tetrazol-2-yl) arm of the first iron(II) ion binds to the neighbouring one through *exo*-located nitrogen atoms N24.

The same linking scheme applies to the neighbouring metal ion, resulting in the formation of a double bridge. Bridging of collinear iron(II) ions occurs in the *c* direction, leading to a polymeric chain (Fig. 3a). Within the polymeric chain, the Fe(II) ions are separated by 9.9917(3) Å and both intrachain contacts, C6–H6(py)–N13(tz^{py}) and C6–H6(py)–N14(tz^{py}), as well as C16–H16B···N23(tz), are present (Table S4). Interactions also occur between polymeric macrocations, such as C17–H17B···N12(tz^{py}). Thus, parallel chains are gathered into layers (Fig. 3c). The area between them is occupied by tetrafluoroborate anions, which are engaged in forming intermolecular contacts with neighbouring layers and extending the structure into a three-dimensional supramolecular architecture (Fig. 3d).

A comparison of the coordination environment of Fe(II) in **2** reveals a similarity to that observed in **1**. Specifically, the two 5-(2-pyridyl)tetrazole chelating fragments, which coordinate through the pyridine nitrogen atoms N1(py) and the tetrazole nitrogen atom N14(tz^{py}), form an equatorial plane.

The remaining two coordination sites are occupied by two tetrazole rings, which coordinate through the nitrogen atom N24(tz). Despite the different position of the (tetrazol-2-yl)propylene arm in 5-p2tz2tz compared to the regioisomeric 5-p1tz2tz, the bridging fashion involving two ligand molecules is the same as that observed in **1**, thus forming a 1D polymeric structure (Fig. 4a). At 100 K, intrachain contacts C18–H18B···N13(tz^{py}) and C6–H6···N13(tz^{py}) are observed (Fig. 4a). Similarly to **1**, anions interact with polymeric chains arranged into supramolecular layers (Fig. 4c).

The thermal stability of **1** and **2** allowed the HS structures to be determined at 480 K. The most significant changes associated with the LS → HS transition are the elongation of the Fe–N distances in **1** and **2** by 0.17–0.22 Å and 0.15–0.17 Å (Table S2), respectively. For both complexes greater deformation of the coordination octahedron is evident in the increase in the $\sum$ value by 22.7° (**1**) and 20.0° (**2**). In **1**, enlargement of the coordination octahedron results in the disappearance of two intrachain C6–H6(py)–N13(tz^{py}) and C6–H6(py)–N14(tz^{py}) contacts (see Fig. 3b and d). Also in **2**, SCO is connected with the disappearance of the intrachain C6–H6···N13(tz^{py}) contact (Fig. 4c). Formation of the HS form is associated with an increase in the separation of the bridged Fe(II) ions in the *c* direction to 10.3075(12) Å in **1** and from 9.8635(7) to 10.078(2) Å in **2**. Additionally, the shortest distances between Fe(II) ions from neighbouring chains increase from 7.9524(3) to 8.2850(18) Å in the *a* direction and from 8.8207(2) to 9.0556(10) Å in the *b* direction. In **2**, distances between Fe(II) ions coming from neighbouring chains increase from 8.5402(4) to 8.8722(24) Å (*a* direction) and from 8.8402(3) to 8.9463(23) Å (*b* direction).

Crystal structures of 3 and 4. Replacing the 5-(2-pyridyl)tetrazole fragment in the ligands of **1** and **2** with 1,2,4-triazole rings yields the isosteric compound 1-(3-(2-pyridyl)-1,2,4-triazol-1-yl)-3-(tetrazol-1-yl)propane. Depending on the solvent used in the synthesis, two isomers of the 1D chain Fe(II) **3** and **4** are obtained.

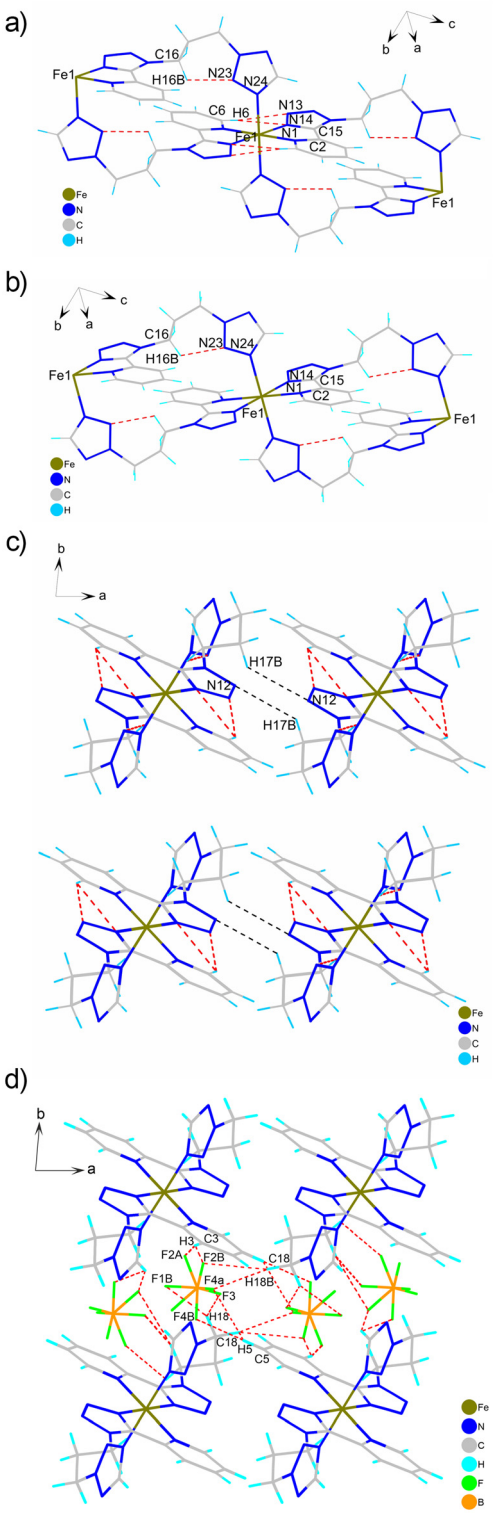

Fig. 3 Coordination environment of iron(II) ions in **1** and the bridging nature occurring within the polymeric chain (a, b) as well as relative arrangement of the polymeric chains (c, d) together with intra- (red dashed lines) and intermolecular contacts (black dashed lines) in the LS (a, c, d) and HS (b) states.

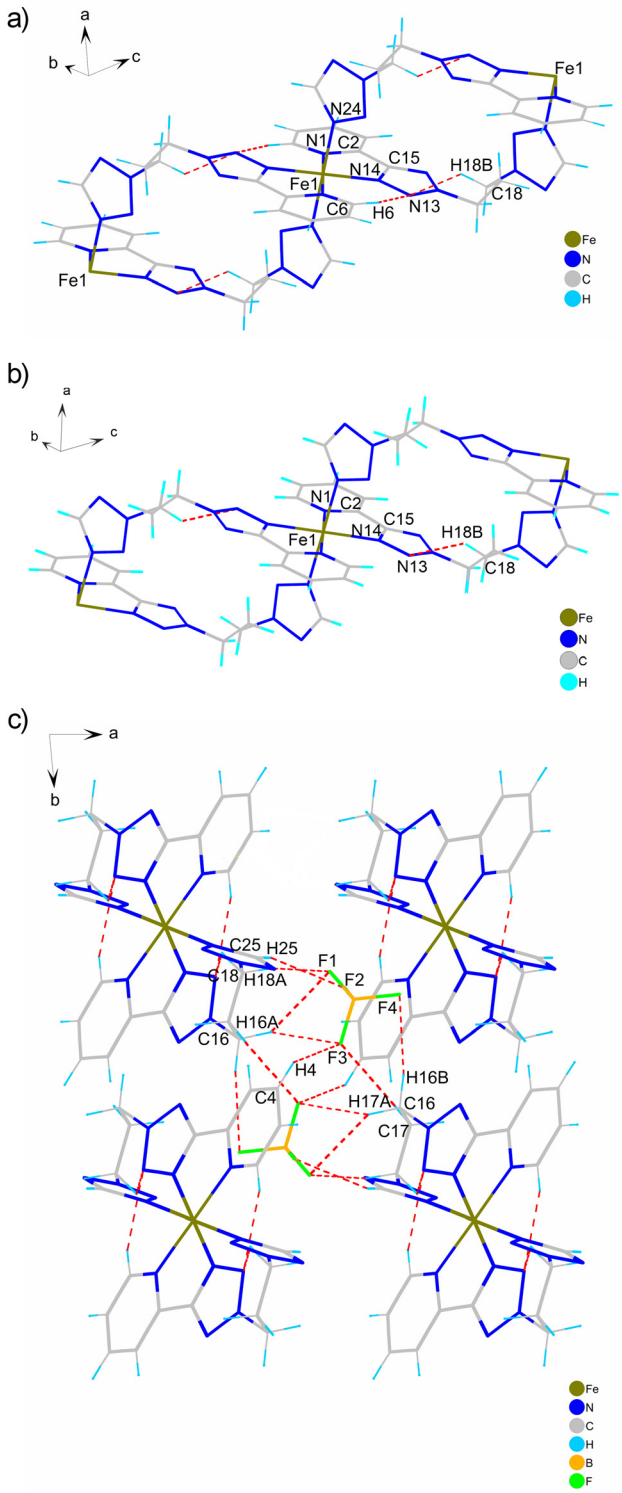

Fig. 4 Coordination environment of iron(II) ions in **2** and the bridging nature occurring within the polymeric chain (a, c) as well as relative arrangement of polymeric chains (b) together with intra- (red dashed lines) and intermolecular contacts (violet dashed lines) in the HS (c) and LS (a, b) states.

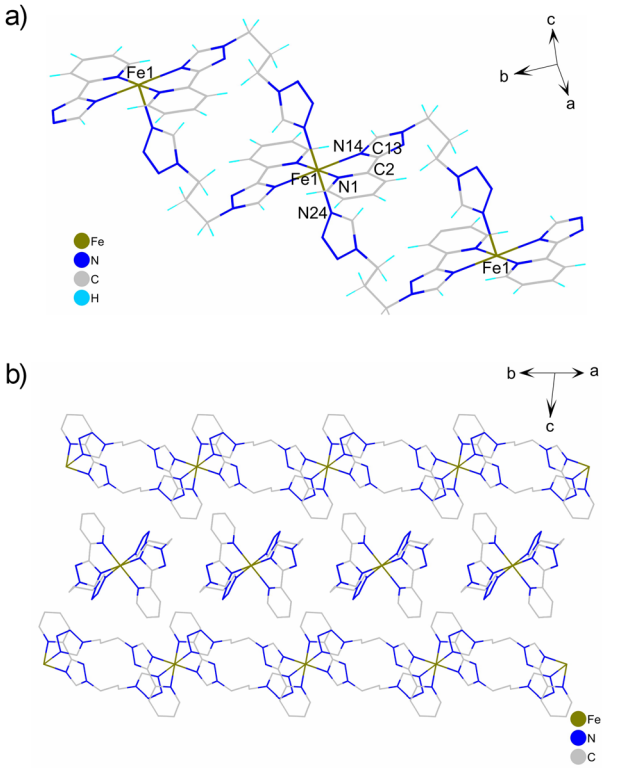

Fig. 5 Coordination environment of iron(II) and the zig-zag shape of the polymeric unit in **3** (a) and view along the [101] direction showing layered arrangement of polymeric chains together with the network of intra- (red dashed lines, a) and intermolecular (black dashed lines) contacts in the HS state (a, b). Green frames (b) denote chains forming supramolecular layers.

3 crystallises in the triclinic $P\bar{1}$ space group. In contrast to **1** and **2**, the tetrazole rings are *cis*-coordinated (Fig. 5). These rings are linked to Fe(II) *via* the nitrogen atoms N24 and N54, and at 250 K, the respective bond lengths are 2.1941(25) and 2.1615(23) Å (see Table S3). Ligand 3-p1tr1tz coordinates through the *endo* nitrogen atoms N14(tr^{py}) and N44(tr^{py}), and the Fe–N distances are equal to 2.1712(23) and 2.1480(23) Å, respectively. Thus, the Fe–N distances are characteristic of the HS form. The N–Fe–N bond angles vary over a wide range, from 75.53(9)° and 75.85(9)° for N(py)–Fe–N(tr^{py}), to 102.08(9)° for N1(py)–Fe–N31(py) (see Table S3).

The pyridyltriazole fragment is almost planar, with the N1(py)–C2–C13–N14(tr^{py}) and N31(py)–C32–C43–N44(tr^{py}) torsion angles measuring 0.019(14) and 1.990(14)°, respectively. The $\sum$ parameter equals 80.48°, which is greater than that observed for **4** (see below). The structure of the first coordination sphere is stabilised by intramolecular C15–H15(tr^{py})···N53(tz) interactions (see Table S5). As with **1**, **2** and **4**, neighbouring Fe(II) ions in **3** are bridged by two ligand molecules; however, the metal ions are not arranged collinearly, which is a crucial difference. This results in the formation of a zig-zag polymeric chain along the [101] direction (Fig. 5a). At 250 K, iron(II) ions linked by two crystallographically independent ligand molecules with different conformations (Table S3)

are separated by 9.9741(6) and 10.1083(14) Å, respectively. The distance between every second Fe(II) ion arranged collinearly along the [101] direction equals 14.7056 Å.

Polymeric chains gathered in the *ab* plane form supramolecular layers. The shortest distance between Fe(II) ions in the adjusted polymeric chains is 8.5753(6) Å, and there are direct intermolecular contacts (C35–H35(py)···N52(tz)) between chains in the same layer (Fig. 5b). Similarly to **1** and **2**, the polymeric chains forming neighbouring layers in **3** are oriented parallel to each other. There are no direct intermolecular contacts between neighbouring layers. The tetrafluoroborate anions participate in the formation of intermolecular contacts (Fig. S4a). The presence of non-coordinating acetonitrile molecules in the space between the layers (see Fig. S4b) is stabilised by intermolecular contacts with the tetrafluoroborate anions. Cooling a crystal of **3** to 80 K results in a shortening of the Fe–N distances by approximately 0.19 Å, indicating a change in the spin state.

It should be noted that SCO involves changes in N–Fe–N bond angles (see Table S3), which result in a reduction in the $\sum$ parameter by 32.9°. The distances between the bridged Fe(II) ions decrease to 9.9547(16) and 9.8793(7) Å (*i.e.* approximately 0.20 Å), and the separation between every second collinearly arranged Fe(II) ion decreases to 14.3967(15) Å. Thus, a change in the spin state triggers the shortening of the polymeric chain.

The shape of the zig-zag chain remains practically unchanged because the Fe–Fe–Fe bond angle drops slightly from 94.15 to 93.08°. Also, the width of the polymeric chain (the distance between the lines defined by the collinearly arranged iron(II) ions) remains practically unaffected. The position of the non-coordinated acetonitrile molecules and tetrafluoroborate anions relative to the polymeric chains changes only slightly.

One of the two crystallographically independent anions remains disordered at 80 K. The formation of the LS structure is accompanied by the formation of novel inter-chain contacts: C6–H6(py)···N44(tz) and C15–H15(tr)···N53(tz) (see Fig. S4a). Also, the C98–H98A···N12(tr) contact between the methyl groups of acetonitrile molecules and macrocationic chains emerges in the LS state (see Fig. S4b). These alterations are associated with a change in the dihedral angle between the average planes of the pyridyltriazole fragments, from 64.4° to 77.1°. An increase in crystal packing is reflected by an increase in the number of intermolecular contacts involving tetrafluoroborate and acetonitrile molecules (see Table S5).

Changing the solvent from acetonitrile to methanol resulted in **4** (*C*2/*c* space group, Table S1). The compound is characterized by a different organization of the first coordination sphere compared to **3**. Similarly to **1** and **2** pyridylazole chelating fragments, coordinated through the N1(py) nitrogen atom of pyridine and the N14(tr^{py}) nitrogen atom of the 1,2,4-triazole ring, form an equatorial plane whereas the axial positions of the coordination octahedron are occupied by tetrazole rings (Fig. 6a). The N1(py)–C2–C13–N14(tr^{py}) torsion angle is 12.526(5)° (see Table S3), indicating a greater degree of twisting of the conjugated rings compared to **1**, **2** and **3**. The Fe–N

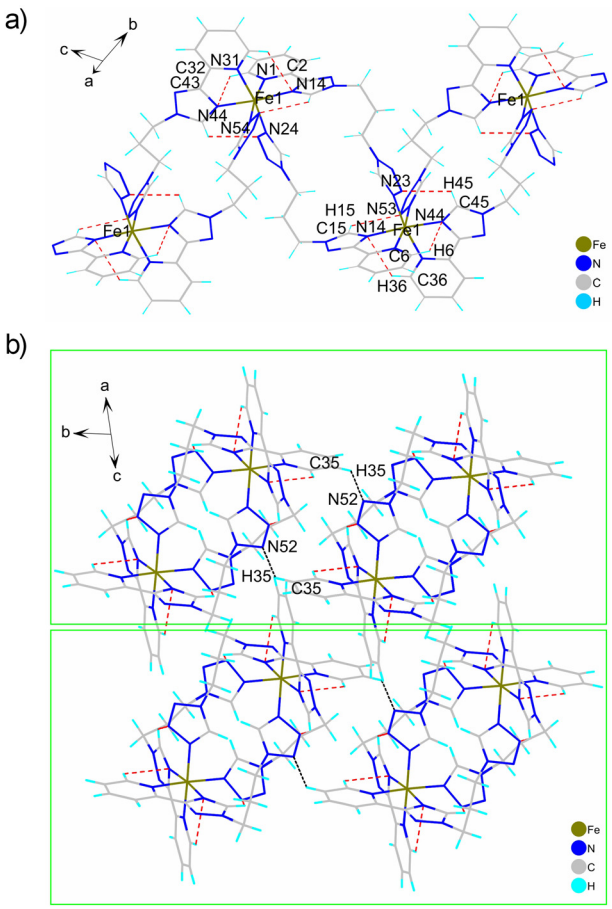

Fig. 6 Coordination environment of iron(II) ions and the bridging nature occurring within the polymeric chain in **4** (a) as well as relative arrangement of polymeric chains (viewed along the [110] direction, hydrogen atoms were omitted for clarity) (b).

distances determined at 250 and 90 K are characteristic of the HS form of the complex (see Table S3). The N–Fe–N bond angles (*e.g.* N1(py)–Fe–N14(tr^{py})) are similar to those found in the HS form of **2**, and the bridging established between collinearly arranged Fe(II) ions is the same as that observed in **1** and **2**. The linked metal ions are separated by 10.1812(3) Å. The chains are oriented parallel to the [110] direction of the formed layers. Nevertheless in contrast to **1**, **2** and **3**, polymeric chains originating from neighbouring layers are oriented along the [−110] direction. Thus, the crystal is built up from alternately arranged, perpendicularly twisted layers (Fig. 6b). In effect, there are two types of channel, which are occupied by either tetrafluoroborate anions or methanol molecules (see Fig. S5). Counterions and methanol molecules engage in the formation of numerous intermolecular contacts (see Table S5). At 90 and 250 K, no intermolecular contacts are observed to be established directly between the atoms of neighbouring polymeric chains.

Comparison of crystal structures of 1–4. A summary of the research results of the SC-XRD studies of **1**, **2** and **4** reveals that they have very similar structures, with the first coordination spheres composed of two pyridylazole chelating frag-

ments that form an equatorial plane, as well as two axially coordinated tetrazole rings. The structures of the polymeric chains of **1**, **2** and **4** are also very similar. A comparison of the geometries of the coordination spheres of the HS forms shows that the $\sum$ parameter is slightly higher for **1** or **2** than it is for **4**, at 65.99° and 64.40°, respectively. It should be noted that the average Fe–N distance for **4** (2.169 Å) is slightly larger than that for compound **2** (2.151 Å). Thus, a comparison of the coordination octahedra of **2** and **4** does not allow us to identify the reason for their significantly different properties. Conversely, the main differences between **2** and **4** can result from different sets of donors (5-(2-pyridyl)tetrazole *vs.* 3-(2-pyridyl)-1,2,4-triazole) and the presence of methanol molecules in the crystal lattice of **4**. Nevertheless, magnetic and SC-XRD studies of **3**, which is based on the same ligand molecule as **4** but has a crystal lattice solvated with acetonitrile instead of methanol, revealed the occurrence of hysteretic thermally induced SCO (Fig. 2b and Fig. S6). This suggests that the donor–acceptor properties of the 1,2,4-triazole-based ligand do not preclude SCO. Furthermore, the SCO temperature of **3** is significantly lower than that of **1** and **2**, suggesting that pyridyl (1,2,4-triazole)-based ligands stabilise the HS form more effectively than 5-(2-pyridyl)tetrazole-based derivatives (**1** and **2**). Comparing the HS forms of **3** and **4** shows that the average Fe–N distances are smaller for **4**. Additionally, the sum of the twelve *cis*-N–Fe–N angles (the $\sum$ value) for **4** is smaller than that for **3**, indicating greater deformation of the coordination sphere of the second system. Hence, contrary to the experimental results, the parameters of the [FeN_6] chromophores should favour the LS form of **4** in relation to **3**, and it can be concluded that the geometry of the coordination sphere of **4** does not prevent SCO from occurring. Both complexes crystallise as acetonitrile or methanol solvates, and comparing the crystal packing of the HS forms of **3** and **4** reveals that the volumes occupied by the complex molecules are almost identical, at 784.2 $Å^3$ (250 K) and 784.3 $Å^3$ (250 K), respectively. Notably, there are two significant structural differences between **3** and **4**. The first is the different arrangement of donors in **3**, where the tetrazole rings are in a *cis* position compared to the *trans* position in **4**, which can result in different ligand fields in **3** and **4** and explain the difference in SCO properties. Secondly, the zig-zag structure of the polymeric chain in **3** differs from the linear polymeric unit in **4**.

In conclusion, the organisation of the first coordination spheres does not appear to be the sole factor determining the ability to undergo thermally induced SCO. Notwithstanding the effects of entropy, this implies the importance of chain structure for spin-transition thermodynamics. To reveal the probable reasons for the differentiation of SCO properties, we carried out DFT modelling of the HS and LS forms of **1–4**, comparing them with different models of mononuclear units.

DFT modelling

The main goal of the DFT modelling of **1–4** was to estimate the effect of 1D-chain formation on electronic spin-transition energies ($E_{el} = E_{el}(HS) - E_{el}(LS)$). First, we considered the calculated model of the 1D chain, and then we compared the obtained E_{el} values with those of the different monomeric unit models (see below). Although no reports on the structures and properties of mononuclear complexes bearing four tetrazole and two pyridine ligands, or two tetrazoles, two pyridines and two triazoles are available, we also applied the results of the above-outlined approach to mononuclear hexa-*n*-propyl *N*-tetrazole and its 1D polynuclear chains derived from 1,3-*N*-tetrazole-propane. We begin by describing the model molecules that were applied and compare the obtained geometries with the experimental ones.

Structural model and obtained geometries

The systems under study correspond to a wide class of one-dimensional (1D) chains of SCO Fe(II) complexes with bridging azole ligands.[24,25]

Modelling such systems to avoid the problems raised by solid-state periodic boundary conditions[26] may be possible for single-molecule calculations involving a polynuclear fragment of the chain. Such models have been proven successful in predicting trends in spin-transition energies and entropies, vibrational properties, and even cooperative behaviour related to interactions within the chain.[17,27] Typically, calculations involved fragments with three to nine metal centres. Here, we applied pentanuclear fragments involving ten anions. Fig. 7 shows an example of a structural model of **1**.

The coordinates for geometry optimisation were taken from the X-ray data. In the case of **1**, the Zn(II) analogue of the LS structure was modelled and optimised prior to the optimisation of the HS Fe(II) complex. The LS model of **4** was optimised starting from the HS structure. Geometry optimisations were performed using the B3LYP functional,[28] the cep-31g basis set[29] and the Grimme D3 dispersion correction,[30] using Gaussian 16.[31] This yielded the electronic energies of both the HS and LS isomers of the pentanuclear models. The results including vibronic effects and the calculated thermodynamic parameters are provided in the SI. The optimised structures are given as PDB files in the SI.

Optimising the geometry of the pentanuclear models reproduced the linear arrangement of the iron centres in chain **1** and the zig-zag arrangement in chain **3**. The linear arrangement

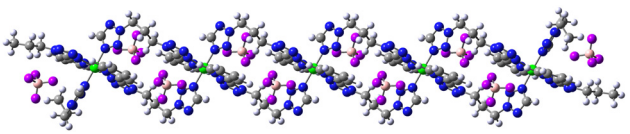

Fig. 7 The model molecule was used for DFT calculations for **1**. Note that the centrosymmetric character of the system is approximately retained for all spin isomers of linear **1**, **2** and **4**. The three inner Fe(II) centres strictly display the environment observed in the X-ray structure. The two terminal centres have the same coordination, but each bis-pyridyltriazole and bis-pyridyltetrazole ligand is cut in half, resulting in an *n*-propyl group. The figure shows the optimised structure of the LS isomer. No solvent molecules present in the crystals were taken into account in the calculations.

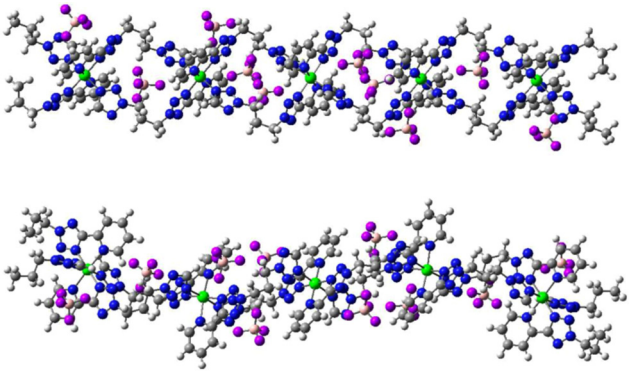

Fig. 8 The optimised geometries of the LS (top) and HS (bottom) isomer models of **2**.

has also been reproduced for the LS model of **2**. For the HS model of **2**, as well as for both spin isomers of **4**, the obtained geometries show a bent chain, with the three inner Fe centres being collinear and the terminal ones bent at approximately 150–160° with respect to the inner three (see Fig. 8).

The calculated Fe–N bond distances for the complexes under study are listed in Table S6. The results obtained are in reasonable agreement with the experimental results. Note that the structures of the linear complex models **1**, **2** and **4** were optimised within the C_i symmetry.

Electronic energies of spin transition for pentanuclear species

The electronic energy of the LS → HS transition (E_{el}) is the difference between the calculated electronic energies of the LS and HS states. It is the main component of the spin-transition energy. As the volume change ($p\Delta V$) for SCO systems is negligible, the spin-transition energy can be considered equivalent to the enthalpy change.[32] The actual spin-transition energy is the sum of E_{el} and the vibrational energy change, which may be a significant part of E_{el} (see SI and ref. 23). The calculated E_{el} values depend on the exchange–correlation functional used, yet the stabilisation trends of a given spin state within a series of complexes are usually reproduced reasonably well.[32–34] The results of the electronic spin-transition energy calculations are presented in Table 1. First, let us look at the results obtained for the pentanuclear models using the B3LYP functional with dispersion corrections (second column in Table 1). Only systems with the same ligand core can be compared, *i.e.* **1** and **2**, and **3** and **4**, respectively. For the latter pair, all three approaches (B3LYP, B3LYP/D3 and B3LYP*) reproduce the experimentally observed high stabilisation of the HS state for **4** compared to the SCO state of **3**. Conversely, the E_{el} values obtained for **1** and **2** differ significantly, despite the transition temperatures for both complexes lying at over 300 K. This energetic difference appears to be offset to some extent by vibrational entropic effects (see the SI).

From cationic mononuclear complex to the polynuclear chains. The effects of structural changes on the calculated spin-transition energies of the model molecules

The data in Table 1 show the spin-transition energies calculated for the different models of molecules **1–4**.

These begin with the isolated dicationic mononuclear models and progress through mononuclear species with two anions to pentanuclear chain models, with and without dispersion correction. These results are shown schematically in

Table 1 The calculated electronic energies (in kJ mol^{-1}) of the full spin transition (with five switching Fe(II) centres) for the pentanuclear and mononuclear models of **1–4** are given, along with the E_{el} data for each Fe(II) centre in the chain (in italics). These energies correspond to geometries optimised using the B3LYP functional and Grimme's dispersion correction, with the cep-31g basis set. Additionally, the values obtained with no dispersion corrections for B3LYP and with B3LYP* for the same geometries are denoted with *. The values for the mononuclear models were obtained from the geometries of the central Fe(II) core of the pentanuclear models, for the mononuclear dications and mononculear complexes with two anions (see Fig. 9). While the choice of anion coordinates for the mononuclear models involving two tetrafluroborate molecules was straightforward for systems **1–3**, two orientations are possible for model **4**, named 'dist' and 'prox'. In the 'dist' orientation, the anions are placed in the plane of the monodentate tetrazole ligand, and in the 'prox' orientation, they are shifted above this plane (see SI, Fig. S7). This results in F–H triazole contacts of less than 2.5 Å or more than 3.0 Å, respectively. Additionally, the E_{el} value for **2** involving the mononuclear complex and four anions was calculated for model **4** (in bold). Finally, the E_{el} values were calculated for the dicationic monomer unit after optimisation (see the sixth column in Table 1)

Compound	E_{el} B3LYP + dispersion[a]	E_{el} B3LYP[b]	E_{el} B3LYP*[b]	E_{el} B3LYP + dispersion		
				Mononuclear cation		
Pentanuclear model				Pentanuclear model geometry	Optimised geometry	Mononuclear cation with two anions[c]
1	109/*22*	87/*17*	207/*41*	23[c]	18[d]	31
2	29/*6*	17/*3*	129/*26*	24[c]	17[d]	33
3	49/*10*	66/*13*	184/*37*	20[c]	8[d]	33.5
4	−6/*−1*	−78/*−15.5*	20/*4*	−4[c]	3[d]	−19 prox[e] +30 dist[e] **−4**[f]

[a] Optimised for the pentanuclear model with B3LYP + D3 dispersion correction. [b] Single-point energy calculation for the geometry of the pentanuclear model optimised with B3LYP + D3 dispersion correction. [c] Single-point energy calculation for the mononuclear fragment with the geometry of the central Fe(1) in the pentanuclear model optimised with B3LYP + D3 dispersion correction. [d] Optimised geometry of the dicationic mononuclear unit starting with the geometry of the central Fe(1) in the pentanuclear model optimised with B3LYP + D3 dispersion correction. [e] Two different orientations of the anion relative to complex cation were considered; see Fig. S7. [f] All four anions were included in the $[FeN_6](BF_4)_4^{2-}$ model.

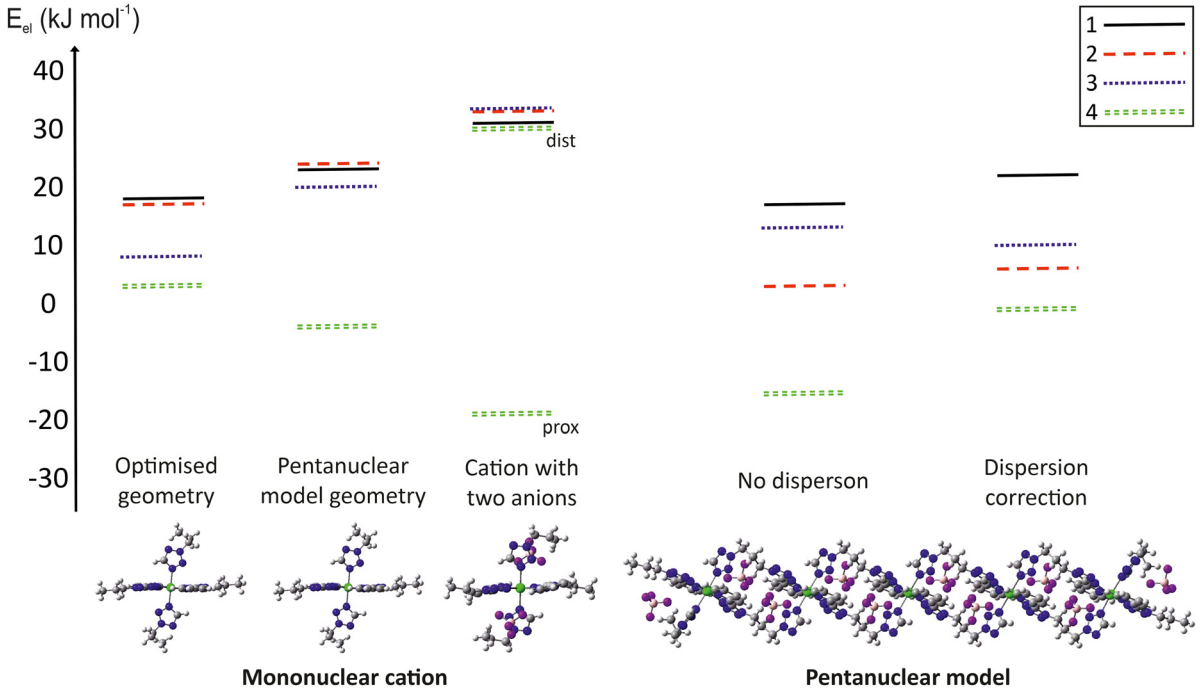

Fig. 9 The dependence of electronic spin-transition energies (for each Fe centre) on the level of modelling of the chain structures of **1–4**. Interestingly, if the solvent molecules of CH_3CN are included in the calculation of the pentanuclear model of **3** (being the next approach to model the interactions seen in the X-ray structure) the E_{el} value for each Fe centre is lowered by *ca.* 1 kJ mol^{-1}.

Fig. 9. When modelling mononuclear systems, both chelating and monodentate tetrazole ligands were modelled with an n-propyl group, as shown in Fig. 10.

We will start by discussing the results for the optimised geometries of the mononuclear dicationic models. The calculated E_{el} values shown in Table 1 (sixth column) align with the observed trend in SCO properties (assuming that the $T_{1/2}$ sequence depends solely on E_{el}). The E_{el} values for **1** and **2** are very close, while the value for **4** is small, indicating relative stabilisation of the HS state. Additionally, E_{el} for **3** is lower than that for **1** and **2**, indicating lower $T_{1/2}$ values, and higher than that for **4**. Comparing these values with those obtained for the monomer geometries corresponding to the pentanuclear models (Table 1, fifth column) reveals an increase in E_{el} for **1–3** and a decrease for **4**. Furthermore, the E_{el} value for **3** approaches that for **1** and **2**. Therefore, the change in the geometry of the mononuclear unit when transitioning from the isolated $[FeN_6]^{2+}$ unit to the chain system solely tunes the ligand-field strength. However, the picture changes if the calculations involve two anions close to the mononuclear unit. These calculations used the above-discussed geometries, with the positions of the BF_4^- anion taken from the optimised structures of the HS and LS models. For **1–3**, the choice of anion was straightforward. For **4**, however, two different pairs of anions were considered (see the caption of Table 1 for details). Including the anions in the E_{el} calculations yielded values of 31–34 kJ mol^{-1} for **1–3** (see Table 1, seventh column), suggesting that the anions stabilise the LS state. The situation is more complex for **4**, where there are two values of electronic energy for both the LS and HS isomers, corresponding to the two different arrangements of the BF_4^- anions found in the optimised structure of the pentanuclear models. E_{el} values of −19 and +30 kJ mol^{-1} were obtained, respectively. Surprisingly, the model involving all four anions around the mononuclear cations yielded a value of −4 kJ mol^{-1}. Overall, the above results suggest a decisive influence of the anions on the effective ligand field.

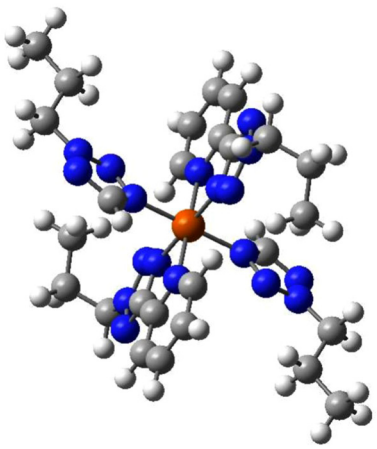

Fig. 10 Example of the mononuclear cationic model used in the DFT calculations.

Calculations of E_{el} for the pentanuclear models of the complexes under study, performed with the B3LYP approach for geometries optimised with the B3LYP/dispersion approach and with no dispersion corrections, illustrate the importance of chain formation for the relative stability of both spin states. One observes a decrease in E_{el} below the values obtained for the models featuring a mononuclear centre with two anions and differentiation of E_{el} for **1–3**. The corresponding modelling was performed using the B3LYP* functional, which is known to increase the stability of the LS state of Fe(II) complexes[34] compared to B3LYP. This modelling reproduces the sequence E_{el} (**1**) > E_{el} (**3**) > E_{el} (**2**) > E_{el} (**4**), which was obtained using B3LYP (see Table 1), yielding values of 20–24 kJ mol^{-1} for **1–3** and −4 kJ mol^{-1} for **4**.

The effect of the formation of the chain on the spin-transition energies can be attributed to interligand interactions and the accumulation of positive charge along the chain. Given its negative contribution to E_{el} (stabilising the HS state), these interactions appear to be predominantly repulsive in nature. Another possible factor is the difference in strain of the bridging ligand between the LS and HS spin isomers. Upon the LS-to-HS transition, the increased volume of the coordination units would result in an overall increase in intermolecular distances, thus reducing repulsion.[28]

The importance of dispersion effects can be seen by comparing B3LYP calculations with and without dispersion corrections. Interestingly, while the dispersion effects appear to increase the stability of the LS state for the pentanuclear models of **1**, **2** and **4** by 22, 12 and 72 kJ mol^{-1}, respectively, the effect for model **3** is the opposite, with E_{el} decreasing by 12 kJ mol^{-1} when dispersion is considered.

It was interesting to perform a similar analysis on a system in which both mononuclear and polynuclear chain modifications display the SCO property. One such system involves propyl-tetrazol ligands, which yield SCO transitions in the hexacoordinated Fe(II) complex[36] and its 1D analogue[37] with 1,3-di(tetrazol-1-yl)propane (**5**), yielding 1D chain complexes that are structurally similar to the systems studied in this paper. Therefore, we performed calculations on different models of complexes involving 1-propyltetrazole ligands, using the approach discussed above for **1–4**. We also calculated the spin-transition energy for the optimised structure of the mononuclear $[Fe(Pr\text{-}tetrazole)_6]^{2+}$ and $[Fe(Pr\text{-}tetrazole)_6](BF_4)_2$. The results, including the optimisation of $[Fe(Pr\text{-}tetrazole)_2](BF_4)_2$, are shown in Fig. 11. The obtained pattern resembles that previously discussed for modelling **1–4**, showing that each modelling step brings a different positive or negative contribution to the E_{el}.

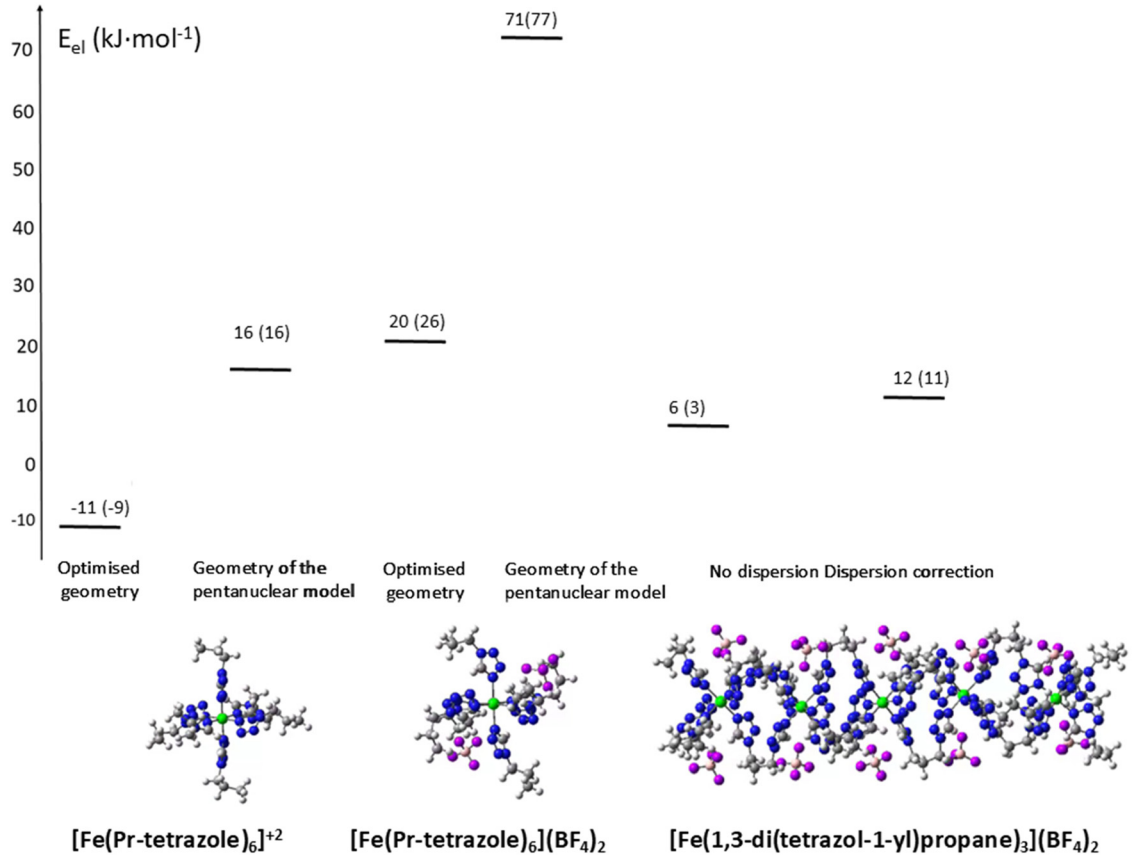

Fig. 11 The E_{el} values (for each Fe centre) of different models of the mononuclear $[Fe(Pr\text{-}tetrazole)_6](BF_4)_2$ and its 1D polynuclear analogue $[Fe(1,3\text{-}di(tetrazol\text{-}1\text{-}yl)propane)_3](BF_4)_2$ modelled as a pentanuclear chain calculated with the B3LYP/D3 and cep-31g basis sets. The values in parentheses are those obtained using the 6-31g basis set.

It is important to note at this point that the calculated E_{el} values are not only dependent on the exchange–correlation functional but also on the basis set.[35] Therefore we performed the calculations for the Pr-tetrazole model molecules with the 6-31g basis set.[36] Similarly to the behaviour observed for **1–4** (with the exception of the monomeric model of **4** with a proximal C–H–F contact), the highest E_{el} is found for the mononuclear unit of the complex with anions in a chain-like geometry. Forming the chain leads to a decrease in E_{el}, which changes moderately when dispersion is accounted for. It is important to note that the effect shown in Fig. 9 does not seem to be related to changes in Fe–N bond distances. The DFT modelling results are consistent with the X-ray data, which show that there are no significant changes in metal–ligand bond distances when going from mononuclear to polynuclear 1D complexes involving the 1-propyltetrazole fragment. The X-ray data give Fe–N bond distances of 1.991 Å (ref. 37) and 1.995/2.004 Å (ref. 38) for the mononuclear and polynuclear 1D molecules, respectively. For the HS isomer, the respective values were found to be 2.185 and 2.182/2.184 Å. DFT modelling of the 1D chains yields values of 2.177 and 1.990 Å, respectively.

The values for the optimised structures of LS $[Fe(ptz)_6]^{2+}$ and LS $[Fe(ptz)_6](BF_4)_2$ are 2.007 and 1.984 Å, respectively, while those for the HS isomer are 2.166 and 2.159 Å.

It is important to note at this point that the calculated E_{el} values are not only dependent on the exchange–correlation functional but also on the basis set.[35] Therefore, we performed the calculations for the Pr-tetrazole model molecules with the 6-31g basis set.[36] The obtained values are indicated in parentheses in Fig. 11. Not only are the trends obtained with both the cep-31g and 6-31g basis sets essentially the same, but the individual E_{el} values are also reasonably close to each other. While we previously showed, by comparing the results of E_{el} calculations using the B3LYP and B3LYP* functionals, that the overall trends are similar, the present comparison suggests that although different basis sets yield different values of E_{el}, the trend for the series of related molecules is nevertheless reproduced (*cf.* ref. 32 and 33*c*).

In summary, DFT modelling shows that changing from mononuclear to polynuclear complexes involving ditopic azole ligands alters the spin-transition energies. First, the geometry of the cation complexes differs between the mononuclear unit and the pentanuclear chain. This implies a change in the ligand field. Second, the difference in anion position between the mononuclear and polynuclear models leads to a further change in the calculated spin-transition energies. The formation of the 1D chain, which brings about intermolecular effects, leads to a further tuning of the spin-transition energies. Meanwhile, the corresponding dispersion interactions typically lead to an increase in E_{el}. We also estimated strain differences by calculating ditopic ligand energies for optimised LS and HS-pentanuclear geometries and determining the mean value for the ligand bound to the central Fe(II) in the chains. We calculated the strain-energy difference, ΔE_{strain}, as the difference between the mean electronic energies of the ligand in the LS and HS states of the optimised modes. The obtained values of ΔE_{strain} are 10, 9, 11 and 15 kJ mol^{-1} for **1**, **2**, **3** and **4**, respectively. This indicates a reduction in ligand strain when transitioning from the LS to the HS state, which is consistent with previous findings for the mononuclear Fe(II) complex with a hexadentate ligand. Conversely, for the pentanuclear model $[Fe(Pr\text{-}tetrazole)_2](BF_4)_2$, ΔE_{strain} was calculated to be −11 kJ mol^{-1}, suggesting that ligand strain is lower in the LS state. Fig. 12 shows the identified effects on structural changes when going from mononuclear cationic through mononuclear complexes with two anions to polynuclear ones involving anions. Modelling the interactions between the ligands and the anions indicates the importance of proximity to the donor properties of the anion. In the case of 3-p1tr1tz, the presence of an anion molecule with a 2.388 Å contact between the closest fluorine and the triazole C–H proton in the presence of a BF_4^- anion (corresponding to the LS isomer of **4** with proxy geometry, see above) results in a σ-character ligand, while an isolated ligand reveals a π-donor character. It appears that the orientation of the anion with respect to the active hydrogens of the ligand is another factor that determines the ligand-field strength. This topic is discussed in detail in the SI. The role of vibronic effects in the thermodynamics of spin transitions is also discussed in the SI.

The values obtained for the electronic spin-transition energies of the applied models of the isolated chain fragment are an alternative to the complex periodic calculations, which themselves pose limitations (*cf.* ref. 23*a*). This model is affected by not factoring in packing effects. It is not immediately clear how including the intermolecular interactions would affect the spin energetics of the chain model. The available data for molecular crystals of mononuclear SCO complexes (ref. 39) show that (i) embedding of the model SCO centre in its crystal lattice brings about the shift of E_{el} at a few kJ mol^{-1} and (ii) this shift is dependent on whether the considered lattice is in the HS or LS state. Consequently, one may expect the few kJ mol^{-1} shift of the E_{el} value when considering the packing effects for the pentanuclear models.

Summary

In this report, we present the application of three ditopic ligands: 1-(5-(2-pyridyl)tetrazol-1-yl)-3-(tetrazol-2-yl)propane (5-p1tz2tz), 1-(5-(2-pyridyl)tetrazol-2-yl)-3-(tetrazol-2-yl)propane (5-p2tz2tz), and 1-(3-(2-pyridyl)-1,2,4-triazol-1-yl)-3-(tetrazol-1-yl)propane (3-p1tr1tz). These ligands are used to prepare one-dimensional Fe(II) coordination polymers. We established that the presence of the pyridyltetrazole fragment in the ligand molecule strongly stabilises the LS form. The complexes $[Fe(5\text{-}p1tz2tz)_2](BF_4)_2$ (**1**) and $[Fe(5\text{-}p2tz2tz)_2](BF_4)_2$ (**2**) exhibit complete thermally induced SCO above room temperature. In contrast, SCO in the complex $[Fe(3\text{-}p1tr1tz)_2](BF_4)_2{\cdot}CH_3CN$ (**3**), which contains ligands with a 1,2,4-triazole ring, occurs at significantly lower temperatures ($T_{1/2}^{\downarrow}$ = 114 K, $T_{1/2}^{\uparrow}$ = 131 K), and the complex $[Fe(3\text{-}p1tr1tz)_2](BF_4)_2{\cdot}CH_3OH$ (**4**) remains in the HS form down to 10 K. **3** and **4** have the same composition in their first coordination spheres; however, their structures

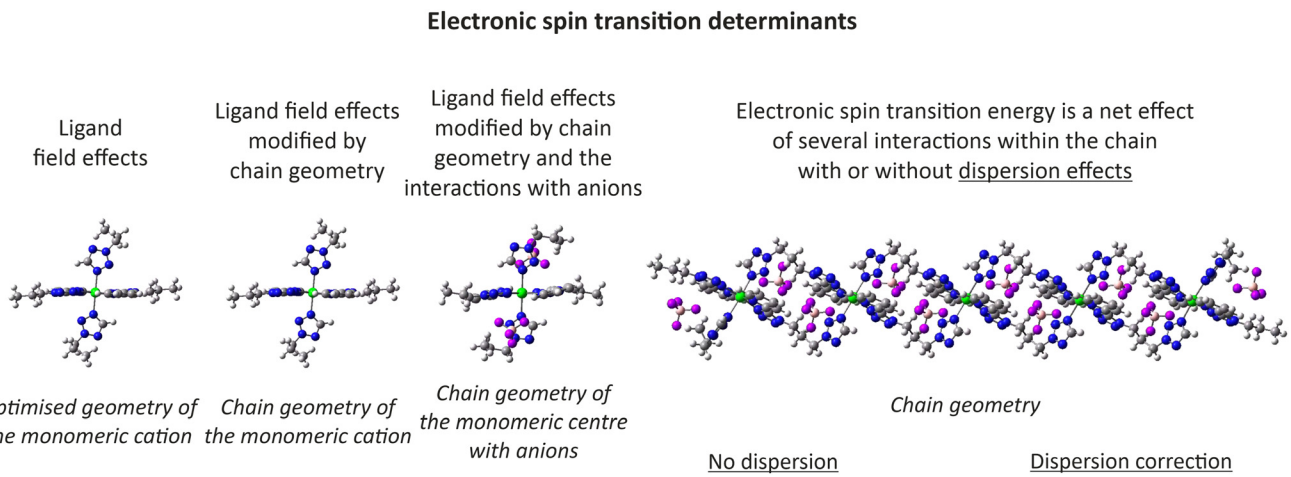

Fig. 12 Several models of the systems under study used to calculate the electronic spin-transition energies and the effects revealed at the different levels of modelling.

differ. Thus, in **3**, the isolated tetrazole rings are *cis*-coordinated, whereas in **4**, similarly to **1** and **2**, they are *trans*-positioned. Furthermore, unlike **1** and **2**, in which iron(II) ions are collinearly arranged in polymeric chains, the polymeric units in **3** are zig-zag-shaped. DFT modelling of pentanuclear chains **1–4**, the $[Fe(Pr\text{-}tetrazole)_6](BF_4)_2$ complex, and their mononuclear subunits revealed complicated changes when transitioning from mononuclear cations to linear chain fragments including anions. For the mononuclear cation, the difference between the optimised geometry and that of the optimised chain units reveals a shift in the calculated electronic spin transition energies, indicating ligand-field modification. The interaction of the mononuclear complex with the anions further modifies the electronic spin transition energy. Several intermolecular interactions and strain upon formation of the chain give rise to a final modification of the E_{el}, with dispersion making a significant contribution. These effects may account for the change in electronic transition energy between the mononuclear cation and the pentanuclear unit, which ranges from −4 kJ mol^{-1} for **4** to +23 kJ mol^{-1} for the hexacoordinate tetrazole complex [Fe(1,3-bis(tetrazol-1-yl) propane)$_3$]BF_4.

Finally, it must be reiterated that, given the limitations of pentanuclear-fragment modelling and the known dependence of calculated spin energetics on the chosen DFT tools, the results presented here should be considered as qualitative rather than quantitative.

Experimental

Materials and methods

The ligands were synthesised according to a method previously reported by us.[20] The acetonitrile used for synthesising the complexes was distilled over calcium hydride. Ethanol was distilled over magnesium ethoxide. Iron(II) tetrafluoroborate hexahydrate was used as supplied (Aldrich) without further purification. Methanol (≥99.9% HPLC grade, Honeywell) was also used without further purification. Elemental analyses for carbon, hydrogen and nitrogen were performed using a CHNS Vario EL III analyser (Elementar). IR spectra of **1–4** were recorded using a 5600 FTIR (Jasco) spectrometer in the range 400–4000 cm^{-1} in Nujol (Alfa Aesar). Temperature-dependent measurements of the magnetic susceptibility of the complexes were carried out with a Quantum Design SQUID magnetometer (MPMS-XL-5) under an applied magnetic field of 1 T. Measurements were carried out at a rate of 1 K min^{-1} (cooling and heating). The magnetic data were corrected for the signal from the glass tube and for the diamagnetic contributions of the sample, estimated from Pascal's constants. DSC measurements (Fig. S3) were performed using a Mettler Toledo DSC at a rate of 5 K min^{-1}. Thermogravimetric analysis was performed using a SETARAM SETSYS 16/18 at a rate of 10 K min^{-1}.

X-ray data collection and structure determination

The crystals of **1–4**, which were suitable for X-ray measurements, were obtained directly from the synthesis of macroscopic samples. They were then preselected using a Zeiss stereoscopic microscope under a nitrogen atmosphere. For the X-ray measurements, single crystals of the complexes were placed on loops and protected by a drop of oil film. Structural studies of **1–4** were performed using a four-circle SuperNova X-ray diffractometer with a microfocus X-ray tube and optimised multilayer optics for Mo Kα (λ = 0.71073 Å) or Cu Kα (λ = 1.54184 Å) radiation, as well as an Atlas CCD detector. The measurement procedure and data reduction were controlled by CrysAlisPro software,[40] which was also used to determine and refine the lattice parameters. Low temperatures were achieved using a stream of cold nitrogen gas (Oxford Cryosystem cooling device), with temperature stability of 0.1 K. The struc-

tures were solved using direct methods. All non-hydrogen atoms were refined using the full-matrix least-squares technique. The hydrogen atoms were modelled as sitting on their parent carbon atoms, with their displacement parameters set to 1.2 or 1.5 times the C or O values. In some cases, the tetrafluoroborate anion and methanol were disordered, so necessary constraints and restraints were applied during refinement (EADP, DFIX, DANG and SUMP). The SHELXS-2013 and SHELXL-2019/2 programs were used for the calculations.[41]

Synthesis of $[Fe(5\text{-}p1tz2tz)_2](BF_4)_2$ (1)

Syntheses of all four coordination compounds were carried out under a nitrogen atmosphere using the standard Schlenk technique. To a solution of 30.9 mg (0.120 mmol) of 5-p1tz2tz in 4.0 ml of ethanol, 20.3 mg (0.0600 mmol) of $Fe(BF_4)_2{\cdot}6H_2O$ in 1.5 ml of ethanol was added. The obtained yellow solution was left in the closed Schlenk flask. After 30 days, red crystals were filtered off and washed with ethanol. Yield 18.5 mg (41.5%). Anal. found: C, 32.5; H, 3.4; N, 33.8%. Calc. for $C_{20}H_{22}B_2F_8FeN_{18}$ (M_w = 743.964 g mol^{-1}): C, 32.3; H, 3.0; N, 33.9%. See Fig. S2a for the IR spectrum.

Synthesis of $[Fe(5\text{-}p2tz2tz)_2](BF_4)_2$ (2)

To a solution of 30.9 mg (0.120 mmol) of 5-p1tz2tz in 4.0 ml of ethanol, 20.3 mg (0.0600 mmol) of $Fe(BF_4)_2{\cdot}6H_2O$ in 1.5 ml of ethanol was added. The obtained pale yellow solution was left in the closed Schlenk flask. After 30 days, red crystals were filtered off. Yield 15.1 mg (33.9%). Anal. found: C, 32.4; H, 3.3; N, 34.0%. Calc. for $C_{20}H_{22}B_2F_8FeN_{18}$ (M_w = 743.964 g mol^{-1}): C, 32.3; H, 3.0; N, 33.9%. See Fig. S2b for the IR spectrum.

Synthesis of $[Fe(3\text{-}p1tr1tz)_2](BF_4)_2{\cdot}CH_3CN$ (3)

To a solution of 30.8 mg (0.120 mmol) of 3-p1tr1tz in 2.5 ml of acetonitrile, 20.3 mg (0.0600 mmol) of $Fe(BF_4)_2{\cdot}6H_2O$ in 1.5 ml of acetonitrile was added. The obtained dark yellow solution was left in the closed Schlenk flask. After 13 days, yellow crystals were filtered off. Yield 15.0 mg (31.9%). Anal. found: C, 37.0; H, 3.5; N, 30.2%. Calc. for $C_{24}H_{27}B_2F_8FeN_{17}$ (M_w = 783.048 g mol^{-1}): C, 36.8; H, 3.5; N, 30.4%. See Fig. S2c for the IR spectrum.

Synthesis of $[Fe(3\text{-}p1tr1tz)_2](BF_4)_2{\cdot}CH_3OH$ (4)

To a solution of 30.8 mg (0.120 mmol) of 3-p1tr1tz in 4.6 ml of methanol, 20.3 mg (0.0600 mmol) of $Fe(BF_4)_2{\cdot}6H_2O$ in 1.0 ml of methanol was added. The obtained yellowish green solution was left in the closed Schlenk flask. After 14 days, green crystals were filtered off. Yield 23.2 mg (50.0%). Anal. found: C, 35.6; H, 3.5; N, 28.9%. Calc. for $C_{23}H_{28}B_2F_8FeN_{16}O$ (M_w = 774.029 g mol^{-1}): C, 35.7; H, 3.7; N, 29.0%. See Fig. S2d for the IR spectrum.

Conflicts of interest

There are no conflicts to declare.

Data availability

The data supporting this article have been included as part of the supplementary information (SI). Supplementary information: Tables S1–S5, Fig. S1–S7 and PDB files of the optimised structures of the pentanuclear models of **1–4**. See DOI: https://doi.org/10.1039/d6dt00320f.

CCDC 2259411, 2259412 (**1**), 2259413, 2259414 (**2**), 2259415, 2259416 (**3**) and 2259417, 2259418 (**4**) contain the supplementary crystallographic data for this paper.[42a–h]

Acknowledgements

V. S. and J. A. W. acknowledge support from the DFG, German Research Foundation—TRR 173-268565370 Spin + X: spin in its collective environment, project A4. V. S. also acknowledges support from the German Ministry of Research (BMBF) under 05K22UK1. J. A. W. and V. S. are grateful to Allianz für Hochleistungsrechnen Rheinland–Pfalz (AHRP) for providing CPU time within the project RPTU-SPINPLUSXA4. V. S. acknowledges support provided by the research initiative NANOKAT.

References

1 (*a*) P. Gütlich, A. Hauser and H. Spiering, *Angew. Chem., Int. Ed. Engl.*, 1994, **33**, 2024; (*b*) J. A. Real, A. B. Gaspar, V. Niel and M. C. Muñoz, *Coord. Chem. Rev.*, 2003, **236**, 121; (*c*) A. Halcrow, *Spin-Crossover Materials: Properties and Applications*, Wiley-VCH, Weinheim, 2013.

2 A. F. Stassen, M. de Vos, P. J. van Koningsbruggen, F. Renz, J. Ensling, H. Kooijman, A. L. Spek, J. G. Haasnoot, P. Gütlich and J. Reedijk, *Eur. J. Inorg. Chem.*, 2000, **10**, 2231–2237.

3 O. Roubeau, M. deVos, A. F. Stassen, R. Burriel, J. G. Haasnoot and J. Reedijk, *J. Phys. Chem. Solids*, 2003, **64**, 1003–1013.

4 (*a*) G.-P. Shen, L. Qi, L. Wang, Y. Xu, J.-J. Jiang, D. Zhu, X.-Q. Liu and X. You, *Dalton Trans.*, 2013, **42**, 10144; (*b*) Y. P. Petrenko, J. Troya, V. García-López, D. M. Khomenko, R. O. Doroshchuk, R. D. Lampeka, M. l Clemente-León and E. Coronado, *Inorg. Chem.*, 2025, **64**(13), 6442.

5 X. Bao, P.-H. Guo, W. Liu, J. Tucek, W.-X. Zhang, J.-D. Leng, X.-M. Chen, I. Guralskiy, L. Salmon, A. Bousseksou and M.-L. Tong, *Chem. Sci.*, 2012, **3**, 1629.

6 (*a*) X. Bao, J.-L. Liu, J.-D. Leng, Z. Lin, M.-L. Tong, M. Nihei and H. Oshio, *Chem. – Eur. J.*, 2010, **16**, 7973; (*b*) J.-B. Lin, W. Xue, B.-Y. Wang, J. Tao, W.-X. Zhang, J.-P. Zhang and X.-M. Chen, *Inorg. Chem.*, 2012, **51**, 9423; (*c*) X. Bao, P.-H. Guo, J.-L. Liu, J.-D. Leng and M.-L. Tong, *Chem. – Eur. J.*, 2011, **17**, 2335.

7 W. Liu, X. Bao, J.-Y. Li, Y.-L. Qin, Y.-C. Chen, Z.-P. Ni and M.-L. Tong, *Inorg. Chem.*, 2015, **54**, 3006.

8 (*a*) W. Liu, X. Bao, L.-L. Mao, J. Tucek, R. Zboril, J.-L. Liu, F.-S. Guo, Z.-P. Ni and M.-L. Tong, *Chem. Commun.*, 2014, **50**, 4059; (*b*) X.-T. Zhang, D. Sun, B. Li, L.-M. Fan, B. Li and P.-H. Wei, *Cryst. Growth Des.*, 2012, **12**, 3845.

9 P.-F. Yao, Y. Tao, H.-Y. Li, X.-H. Qin, D.-W. Shi, F.-P. Huang, Q. Yu, X.-X. Qin and H.-D. Bian, *Cryst. Growth Des.*, 2015, **15**, 4394.

10 H. L. C. Feltham, A. S. Barltrop and S. Brooker, *Coord. Chem. Rev.*, 2017, **344**, 26.

11 G. Aromi, L. A. Barrios, O. Roubeau and P. Gamez, *Coord. Chem. Rev.*, 2011, **255**, 485.

12 J. Kusz, H. Spiering and P. Gutlich, *J. Appl. Crystallogr.*, 2000, **33**, 201.

13 J. Kusz, P. Gutlich and H. Spiering, in *Spin Crossover in Transition Metal Compounds*, ed. H. A. Goodwin and P. Gütlich, Top. Curr. Chem., 2004, vol. 234, p. 129.

14 L. H. Böttger, A. Chumakov, C. M. Grünert, P. Gütlich, J. Kusy, H. Paulsen, U. Ponkratz, V. Rusanov, A. X. Trautwein and J. A. Wolny, *Chem. Phys. Lett.*, 2006, **429**, 189.

15 A. Absmeier, M. Bartel, C. Carbonera, G. N. L. Jameson, P. Weinberger, A. Caneschi, K. Mereiter, J.-F. Letard and W. Linert, *Chem. – Eur. J.*, 2006, **12**, 2235.

16 J. Schweifer, P. Weinberger, K. Mereiter, M. Boca, C. Reichl, G. Wiesinger, G. Hilscher, P. J. van Koningsbruggen, H. Kooijman, M. Grunert and W. Linert, *Inorg. Chim. Acta*, 2002, **339**, 297.

17 S. Rackwitz, W. Klopper, V. Schünemann and J. A. Wolny, *Phys. Chem. Chem. Phys.*, 2013, **15**, 15450.

18 M. Weselski, M. Książek, P. Mess, J. Kusz and R. Bronisz, *Chem. Commun.*, 2019, **55**, 7033.

19 M. Książek, M. Weselski, A. Dreczko, V. Maliuzhenko, M. Kaźmierczak, A. Tołoczko, J. Kusza and R. Bronisz, *Dalton Trans.*, 2020, **49**, 9811.

20 A. Białońska and R. Bronisz, *Tetrahedron*, 2008, **64**, 9771.

21 J. A. Wolny, V. Schünemann, Z. Nemeth and G. Vankö, *C. R. Chim.*, 2018, **21**, 1152.

22 D. C. Ashley and E. Jakubikova, *Coord. Chem. Rev.*, 2017, **337**, 97.

23 (*a*) J. A. Wolny, X. Li, M. Dirtu, K. Gröpl, T. Hochdörffer, H. Paulsen, Y. Garcia and V. Schünemann, *RSC Adv.*, 2025, **15**, 32009 and references therein (*b*) G. Paveliuc and M. Lawson Daku, *J. Phys. Chem.*, 2024, **128**, 8404.

24 P. J. van Koningsbruggen, *Top. Curr. Chem.*, 2004, **233**, 123.

25 Y. Garcia, V. Niel, M. C. Muñoz and J. A. Real, in *Spin Crossover in Transition Metal Compounds*, ed. P. Gütlich and H. A. Goodwin, Top. Curr. Chem., 2004, vol. 233, p. 229.

26 H. Paulsen, V. Schünemann and J. A. Wolny, *Eur. J. Inorg. Chem.*, 2013, **5–6**, 628 and references therein.

27 (*a*) J. A. Wolny, S. Rackwitz, K. Achterhold, Y. Garcia, K. Muffler, A. D. Naik and V. Schünemann, *Phys. Chem. Chem. Phys.*, 2010, **12**, 14782; (*b*) S. Rackwitz, J. A. Wolny, K. Muffler, K. Achterhold, R. Rüffer, Y. Garcia, R. Diller and V. Schünemann, *Phys. Chem. Chem. Phys.*, 2012, **14**, 14650; (*c*) J. A. Wolny, I. Faus, J. Marx, R. Rüffer, A. I. Chumakov, K. Schlage, H.-C. Wille and V. Schünemann, *Magnetochemistry*, 2016, **2**, 19; (*d*) K. Jenni, L. Scherthan, I. Faus, J. Marx, C. Strohm, M. Herlitschke, H.-C. Wille, P. Würtz, V. Schünemann and J. A. Wolny, *Phys. Chem. Chem. Phys.*, 2017, **19**, 18880; (*e*) J. A. Wolny, T. Hochdörffer, S. Sadashivaiah, H. Auerbach, K. Jenni, L. Scherthan, A. M. Li, C. von Malotki, H.-C. Wille, E. Rentschler and V. Schünemann, *J. Phys.: Condens. Matter*, 2021, **33**, 034004.

28 A. D. Becke, *J. Chem. Phys.*, 1993, **98**, 5648.

29 (*a*) W. J. Stevens, H. Basch and J. Krauss, *J. Phys. Chem.*, 1984, **81**, 6026; (*b*) W. J. Stevens, J. Krauss, M. Basch and P. G. Jasien, *Can. J. Chem.*, 1992, **70**, 612; (*c*) T. R. Cundari and W. J. Stevens, *J. Chem. Phys.*, 1993, **98**, 5555.

30 S. Grimme, J. Antony, S. Ehrlich and H. Krieg, *J. Chem. Phys.*, 2010, **132**, 154104.

31 M. J. Frisch, G. W. Trucks, H. B. Schlegel, G. E. Scuseria, M. A. Robb, J. R. Cheeseman, G. Scalmani, V. Barone, G. A. Petersson, H. Nakatsuji, X. Li, M. Caricato, A. V. Marenich, J. Bloino, B. G. Janesko, R. Gomperts, B. Mennucci, H. P. Hratchian, J. V. Ortiz, A. F. Izmaylov, J. L. Sonnenberg, D. Williams-Young, F. Ding, F. Lipparini, F. Egidi, J. Goings, B. Peng, A. Petrone, T. Henderson, D. Ranasinghe, V. G. Zakrzewski, J. Gao, N. Rega, G. Zheng, W. Liang, M. Hada, M. Ehara, K. Toyota, R. Fukuda, J. Hasegawa, M. Ishida, T. Nakajima, Y. Honda, O. Kitao, H. Nakai, T. Vreven, K. Throssell, J. A. Montgomery Jr., J. E. Peralta, F. Ogliaro, M. J. Bearpark, J. J. Heyd, E. N. Brothers, K. N. Kudin, V. N. Staroverov, T. A. Keith, R. Kobayashi, J. Normand, K. Raghavachari, A. P. Rendell, J. C. Burant, S. S. Iyengar, J. Tomasi, M. Cossi, J. M. Millam, M. Klene, C. Adamo, R. Cammi, J. W. Ochterski, R. L. Martin, K. Morokuma, O. Farkas, B. Foresman and D. J. Fox, *Gaussian 16, Revision A.03*, Gaussian, Inc., Wallingford CT, 2016.

32 H. Paulsen and A. X. Trautwein, *Top. Curr. Chem.*, 2004, **235**, 197.

33 (*a*) H. Paulsen, V. Schünemann and J. A. Wolny, *Eur. J. Inorg. Chem.*, 2013, **5–6**, 628 and references therein (*b*) K. P. Kepp, *Inorg. Chem.*, 2016, **55**, 2717; (*c*) S. R. Mortensen and K. P. Kepp, *J. Phys. Chem. A*, 2015, **119**, 4041.

34 (*a*) M. Reiher, O. Salomon and B. A. Hess, *Theor. Chem. Acc.*, 2001, **107**, 48; (*b*) O. Salomon, M. Reiher and B. A. Hess, *J. Chem. Phys.*, 2002, **117**, 4729.

35 M. Güell, J. M. Luis, M. Solà and M. Swart, *J. Chem. Phys.*, 2008, **112**(28), 6384.

36 V. A. Rassolov, M. A. Ratner, J. A. Pople, P. C. Redfern and L. A. Curtiss, *J. Comput. Chem.*, 2001, **22**, 976 and references therein.

37 J. Kusz, H. Spiering and P. Gütlich, *J. Appl. Crystallogr.*, 2000, **33**, 201.

38 (*a*) M. Weselski, M. Książek, J. Kusz, A. Białońska, D. Paliwoda, M. Hanfland, M. Rudolf, Z. Ciunik and

R. Bronisz, *Eur. J. Inorg. Chem.*, 2017, **8**, 1171; (*b*) D. Müller, C. Knoll, B. Stöger, W. Artner, M. Reissner and P. Weinberger, *Eur. J. Inorg. Chem.*, 2013, **5–6**, 984.

39 J.-G. Becker, S. Sundaresan, T. Höchdörffer, J. A. Wolny, L. M. Carella, V. Schünemann and E. Rentschler, *Dalton Trans.*, 2026, **55**, 2833.

40 *CrysAlisPro, Version 1.171.38.41q*, Rigaku Oxford Diffraction, 2015.

41 G. M. Sheldrick, *Acta Crystallogr., Sect. C: Struct. Chem.*, 2015, **71**, 3.

42 (*a*) CCDC 2259411: Experimental Crystal Structure Determination, 2026, DOI: 10.5517/ccdc.csd.cc2fv37n; (*b*) CCDC 2259412: Experimental Crystal Structure Determination, 2026, DOI: 10.5517/ccdc.csd.cc2fv38p; (*c*) CCDC 2259413: Experimental Crystal Structure Determination, 2026, DOI: 10.5517/ccdc.csd.cc2fv39q; (*d*) CCDC 2259414: Experimental Crystal Structure Determination, 2026, DOI: 10.5517/ccdc.csd.cc2fv3br; (*e*) CCDC 2259415: Experimental Crystal Structure Determination, 2026, DOI: 10.5517/ccdc.csd.cc2fv3cs; (*f*) CCDC 2259416: Experimental Crystal Structure Determination, 2026, DOI: 10.5517/ccdc.csd.cc2fv3dt; (*g*) CCDC 2259417: Experimental Crystal Structure Determination, 2026, DOI: 10.5517/ccdc.csd.cc2fv3fv; (*h*) CCDC 2259418: Experimental Crystal Structure Determination, 2026, DOI: 10.5517/ccdc.csd.cc2fv3gw.